

# Saturation of Elliptic flow at RHIC : Results from the covariant elastic parton cascade model MPC

Denes Molnar<sup>1,2</sup> and Miklos Gyulassy<sup>1,2,3</sup>

<sup>1</sup>Physics Department, Columbia University, 538 West 120th Street, New York, NY 10027

<sup>2</sup>RMKI Research Institute for Particle and Nuclear Physics, P.O. Box 49, H-1525 Budapest, Hungary

<sup>3</sup>Collegium Budapest, Szentharomsag u. 2., H-1014 Budapest, Hungary

Differential elliptic flow and particle spectra are calculated using the MPC elastic parton cascade model for Au+Au at  $E_{cm} = 130$  A GeV out to  $p_T = 5$  GeV/c. The evolution is computed from the parton transport theory, followed by hadronization either via independent fragmentation or by imposing parton-hadron duality. With typical few mb elastic cross sections, very large initial gluon densities,  $dN_{g=d} = d = 15000$ , are required to reproduce the preliminary data of STAR and PHENIX at RHIC. Alternatively, the data can be reproduced assuming more moderate  $dN_{g=d} = d = 1000$ , but with much larger elastic cross sections. In addition, we show that the computed spectra and elliptic flow are very sensitive to the numerical particle subdivision necessary to retain Lorentz covariance. Computationally demanding parton subdivisions of  $100 - 1000$  are required to obtain reliable solutions to the ultra-relativistic transport equation for initial conditions expected at RHIC.

PACS 12.38Mh; 24.85.+p; 25.75.-q

## I. INTRODUCTION

Differential elliptic flow,  $v_2(p_T) = \cos(2\phi) i_{p_T}$ , the second Fourier moment of the azimuthal momentum distribution for fixed  $p_T$ , is one of the important experimental probes of collective dynamics in A+A reactions [1]-[13]. The discovery [14] of a factor of two enhancement of elliptic flow in noncentral nuclear collisions at RHIC relative to SPS [15] has generated even more interest in this "barometric" measure of collective transverse flow. In addition, preliminary STAR data reported in [16] suggest a remarkable saturation property of this flow at high  $p_T$  with  $v_2(p_T > 2 \text{ GeV}) \approx 0.15$ . This corresponds to a factor of two azimuthal angle asymmetry of high- $p_T$  particle production relative to the reaction plane. This collective effect depends strongly on the dynamics in a heavy ion collision and therefore should provide important constraints about the density and effective energy loss of partons.

Predictions of collective elliptic flow in non-central nuclear collisions were first based on ideal (nondissipative) hydrodynamics [1,2,6]. Unlike at lower energies, ideal hydrodynamics seems to reproduce the (low  $p_T < 2 \text{ GeV}$ ) data [14] at RHIC remarkably well. However, it fails to saturate at high  $p_T > 2 \text{ GeV}$  as indicated by the preliminary data [16]. The hydrodynamic results was found in [6] to be surprisingly insensitive to the choice of ini-

tial conditions, equation of state and freezeout criteria, once the observed  $dN_{ch=d}$  was reproduced, leaving no adjustable hydrodynamic model parameters with which the saturation property could be reproduced.

The lack of saturation in ideal hydrodynamics is of course due to the assumption that local equilibrium can be maintained until a sudden freeze-out hypersurface is reached. This idealization is certainly too strong outside some finite domain of phase space in heavy ion collisions [17]. The finite transition rates can be expected to produce non-equilibrium deviations from the predicted hydrodynamic flow pattern. Covariant Boltzmann transport theory provides a convenient framework to estimate dissipative effects. The assumption of local equilibrium is replaced by the assumption of a finite local mean free path  $(s; x) = 1 = (s)n(x)$ . The theory then naturally interpolates between free streaming ( $\tau = 1$ ) and ideal hydrodynamics ( $\tau = 0$ ).

The previous calculations of collective flow from covariant transport theory [18-20] lead to too small collective effects. This was probably due to the use of perturbative QCD cross sections and assumed more dilute parton initial densities based on HIJING [21]. Recently, denser parton initial conditions were suggested based on gluon saturation models [22]. Initial gluon densities up to  $\nu$  times higher than from HIJING were predicted. The question studied in this paper is whether such initial conditions may be dense enough to generate the observed collective flow even with pQCD elastic cross sections. In this study, we explore the dependence of elliptic flow on initial conditions, or equivalently<sup>1</sup>, on the magnitude of partonic cross section.

We note that hadronic cascade models supplemented with string dynamics [4,10,11] also underpredict elliptic flow because the spatial asymmetry is too small after hadronization to generate the observed momentum space asymmetry. The reason is that hadronization through strings reduces the strength of partonic level elliptic flow.

The saturation and eventual decrease of  $v_2$  at high  $p_T$  has so far only been predicted as a consequence of inelastic parton energy loss [2,13]. These calculations assume however the validity of an Eikonal approach at moderate  $p_T = 10 \text{ GeV}$ . In addition, the pQCD computable

<sup>1</sup> The equivalence is due to the scaling property explained in Section IIB.

jet quenched part has to be grafted phenomenologically onto an effective "soft" non-perturbative component below  $p_T < 2 \text{ GeV}/c$ . Covariant transport theory is the only self-consistent tool to address simultaneously both the soft collective component and the far from equilibrium high- $p_T$  component. While the available parton cascade models lack a technical means to implement covariant inelastic energy loss, it is of considerable interest to solve elastic parton cascade transport theory to get insight into the possible dynamical interplay between these two components. For large enough elastic opacities the collective flow strength can certainly be reproduced [20]. The outstanding question we focus on is whether the deviation of hydrodynamic flow and its saturation at high  $p_T$  can also be understood in this dynamical framework.

Forerunners of this study [18,20] computed elliptic flow for partonic systems starting from initial conditions expected at RHIC. In this paper we extend those studies in three aspects. We compute the  $p_T$ -differential elliptic flow  $v_2(p_T)$ . The consequences of hadronization are investigated, which is necessary to compare to the observations. Finally, we use realistic di-nucleon geometry for the initial conditions.

We compute the partonic evolution with MPC [23], a newly formulated, covariant, parton kinetic theory technique. MPC is an extension of the covariant parton cascade algorithm, ZPC [24]. Both MPC and ZPC have been extensively tested [25,26] and compared to analytic transport solutions and covariant Euler and Navier-Stokes dynamics in 1+1D geometry. A critical feature of both these algorithms is the implementation of the parton subdivision technique proposed by Pang [26,27].

Extensions of MPC to include inelastic 2  $\leftrightarrow$  3 partonic processes [19] are under development. In this paper, we apply MPC in the pure elastic parton interactions mode as in ZPC [28].

## II. COVARIANT PARTON TRANSPORT THEORY

### A. Transport equation

We consider here, as in Refs. [27,24,23,17], the simplest form of Lorentz-covariant Boltzmann transport theory in which the on-shell phase space density  $f(\mathbf{x};p)$ , evolves with an elastic  $2 \leftrightarrow 2$  rate as

$$\begin{aligned} \frac{d}{dt} f_1(\mathbf{x};p_1) = & \int \int \int (f_3 f_4 - f_1 f_2) W_{12 \rightarrow 34}^4(p_1 + p_2, \mathbf{p}, \mathbf{q}) \\ & + S(\mathbf{x};p_1); \end{aligned} \quad (1)$$

Here  $W$  is the square of the scattering matrix element, the integrals are shorthands for  $\int \frac{g d^3 p_i}{(2\pi)^3 E_i}$ , where  $g$  is the number of internal degrees of freedom, while  $f_j = f(\mathbf{x};p_j)$ . The initial conditions are specified by the

source function  $S(\mathbf{x};p)$ , which we discuss later in Section III.

For our applications below, we interpret  $f(\mathbf{x};p)$  as describing an ultrarelativistic massless gluon gas with  $g = 16$  (8 colors, 2 helicities). We neglect quark degrees of freedom because at RHIC gluons are more abundant.

In principle, the transport equation (1) could be extended for bosons with the substitution  $f_1 f_2 \rightarrow f_1 f_2 (1 + f_3)(1 + f_4)$  and a similar one for  $f_3 f_4$ . In practice, no covariant algorithm yet exists to handle such nonlinearities. We therefore limit our study to quadratic dependence of the collision integral on  $f$ .

The elastic gluon scattering matrix elements in dense parton systems are modeled by a Debye-screened form

$$\frac{d}{dt} = \sigma_0 \left[ 1 + \frac{2}{s} \frac{2}{(t + 2)^2} \right]; \quad (2)$$

where  $\sigma_0$  is the screening mass,  $\sigma_0 = 9 \frac{2}{s} = 2 \frac{2}{s}$  is the total cross section, which we chose to be independent of energy. For small values of  $\sigma_0$ , forward-peaked scattering is favored, while as  $\sigma_0$  increases the angular distribution becomes more and more isotropic. For a fixed total cross section<sup>2</sup>, the relevant transport cross section is

$$\begin{aligned} \sigma_{\text{tr}} &= \int \int \frac{d\Omega}{4\pi} \sin^2 \theta \frac{d\sigma_{\text{el}}}{dt} \frac{4t}{s} \left[ 1 - \frac{t}{s} \right] \\ &= \sigma_0 4z(1+z) [(2z+1) \ln(1+1/z) - 2]; \end{aligned} \quad (3)$$

where  $z = \frac{2}{s} = s$  and  $s$  is replaced by  $hs = 17T_0^2$ . This is a monotonic function of  $\sigma_0$  and maximal in the isotropic ( $\sigma_0 \rightarrow 1$ ) case. In the small angle dominated limit, with  $z \rightarrow 1$ ,  $\sigma_{\text{tr}} = \sigma_0 4z(\ln 1/z - 2)$ .

It is important to emphasize that while the cross section suggests a geometrical picture of action over finite distances, we use Eq. (2) only as a convenient parametrization to describe the effective local transition probability,  $W$ . In the present study this is simply modeled as  $dW = dt = s d\tau = dt$ . The particle subdivision technique (see next Subsection) needed to recover covariance removes all notion of nonlocality in this approach, just like in hydrodynamics. Thus, the cross sections, e.g., 100 mb, used in the present study to simulate a high collision rate do not imply acausal action at a distance.

### B. Parton Subdivision

We utilize the parton cascade method to solve the Boltzmann transport equation (1). A critical drawback of all cascade algorithms is that they inevitably lead to

<sup>2</sup> To keep the total cross section constant as a function of  $\sigma_0$ , one of course has to adjust the coupling  $g$  accordingly.

numerical artifacts because they violate Lorentz covariance. This occurs because particle interactions are assumed to occur whenever the distance of closest approach (in the relative c.m.) is  $d < \frac{d_0}{\gamma}$ , which corresponds to action at a distance.

A causal (superluminal) propagation due to action at a distance leads to severe numerical artifacts. In particular, the transverse energy evolution  $dE_t = dy(\dots)$  and the final asymptotic transverse energy per unit rapidity are frame dependent [17].

To recover the local character of equation (1) and hence Lorentz covariance, it is essential to use the parton subdivision technique [27,24]. This technique is based on the covariance of Eq. (1) under the transformation

$$f \rightarrow f^0, \quad W \rightarrow W^0, \quad W = \gamma (W^0 + \beta^0 \dots): \quad (4)$$

The magnitude of numerical artifacts is governed by the diluteness of the system  $\frac{dN}{dy} = M_{FP}$ , which scales with  $1/\gamma$  [26]. Lorentz violation therefore formally vanishes in the  $\gamma \rightarrow 1$  limit. In practice, very high  $100 - 1000$  subdivisions are needed [17] to obtain accurate numerical solutions of the transport equation (1) from initial conditions expected at RHIC.

### C. Scaling of the transport solutions

Subdivision covariance (4) actually implies that the transport equation has a broad dynamical range, and the solution for any given initial condition and transport property immediately provides the solution to a broad band of suitably scaled initial conditions and transport properties. This is because solutions for problems with  $\gamma$  times larger the initial density  $dN = d^2x_T$ , but with one  $\gamma$ -th the reaction rate can be mapped to the original ( $\gamma = 1$ ) case for any  $\gamma$ . We must use subdivision to eliminate numerical artifacts. However, once that is achieved, we have actually found the solution to a whole class of suitably rescaled problems.

The dynamical range of the transport equation (1) is further increased by its covariance under coordinate and momentum rescaling [17], leading to covariance of the transport theory under

$$\begin{aligned} f(x;p) &\rightarrow f^0(x;p) \quad \frac{1}{\gamma^3} f\left(\frac{x}{\gamma}; \frac{p}{\gamma}\right); \\ W(fp_i;g) &\rightarrow W^0(fp_i;g) \quad \frac{1}{\gamma^2} W\left(\frac{p_i}{\gamma}; \frac{p}{\gamma}\right); \\ m &\rightarrow m^0 = m/\gamma; \end{aligned} \quad (5)$$

where  $x$  and  $p$  are the coordinate and momentum scaling parameters, respectively. This means [17] that we can scale one solution to others provided that both  $\tau_0$  and  $d_0 dN = d$  remain the same (we cannot exploit coordinate scaling because the nuclear geometry is fixed). For example, three times the density with one-third the

cross section leaves both parameters the same, hence the results can be obtained via scaling without further computation.

In general the numerical (cascade) solution of Eq. (1) tends in the  $\gamma \rightarrow 1$  limit toward a covariant physical solution that depends on two scales,  $\tau_0$  and  $d_0 dN = d$ . In an Eikonal picture of high- $p_T$  production, the distributions are expected to depend on the opacity or the mean number of collisions in the medium

$$\begin{aligned} \ln i &= \frac{L}{e_1} = \int dt \frac{d e_1}{dt} dz \quad z; \quad = \frac{z}{c} \\ \frac{dN}{dy} &= \frac{e_1}{2 R_G^2} \log \frac{R_G}{d_0}; \end{aligned} \quad (6)$$

where  $d_0$  is the formation proper time and  $R_G$  is the effective Gaussian transverse coordinate rms radius.

However, from the point of view of dissipative dynamics via Navier-Stokes and Fokker-Planck equation, the more relevant dynamical parameter is the effective transport opacity

$$\frac{t}{e_1} \ln i = \int dz \quad x_0 + z \ln; \quad = \frac{z}{c} i; \quad (7)$$

The ensemble average over initial coordinates and directions is implied above.

In general, the transport opacity is a dynamical quantity that we do not know until we solved the transport equation for the set of parameters  $b$ ,  $d_0 dN(0) = d$ , and  $\tau = \tau_0$  (or equivalently,  $\tau = T_0$ ). However, as we can see from Table I, for the range of parameters considered in this study it is (within 10% accuracy) proportional to the product of the two scales  $d_0 dN(0) = d$  and  $\tau = \tau_0$ :

$$(b; \frac{dN(0)}{d}; \frac{\tau}{\tau_0}) \approx \text{const} \quad \frac{dN(0)}{d} C(b); \quad (8)$$

The nontrivial, in fact parameter dependent part  $C(b)$  is the number of collisions per parton as a function of  $b$  with  $d_0 dN(0) = d$  and  $\tau = T_0$  kept fixed. It is tabulated, for example, in section E) in Table I, in which case the corresponding proportionality constant is  $(\tau dN(0) = d)^{-1} = (0.91 \text{ mb}^{-2} 210)^{-1}$ .

Of course, there is no a priori guarantee that the solutions of Eq. (1) depend only on this transport opacity parameter. However, as we will demonstrate numerically below, this seems to be the case to within 10-20% accuracy for elliptic flow and the transverse momentum spectra out to 6 GeV/c for the parameters and initial conditions appropriate at RHIC energies.

## III. NUMERICAL RESULTS FOR THE PARTONIC EVOLUTION

In this Section we present elliptic flow results and  $p_T$  spectra for the partonic evolution.

Under the scaling (5) the differential elliptic flow  $v_2(p_T)$  and the  $p_T$  spectrum transform as

$$v_2(p_T) \propto v_2^0(p_T) \propto \frac{p_T}{p} \quad (9)$$

$$\frac{dN}{d^2p_T}(p_T) \propto \frac{dN^0}{d^2p_T}(p_T) = \frac{dN}{d^2p_T} \frac{p_T}{p} \quad ;$$

Hence elliptic flow depends on  $p_T$  and  $dN/d^2p_T$  only through the product  $p_T dN/d^2p_T$ . On the other hand, the  $p_T$  spectrum depends on  $p_T$  and  $dN/d^2p_T$  separately.

For Au+Au collisions, the initial condition was taken to be a longitudinally boost invariant Bjorken tube in local thermal equilibrium at temperature  $T_0$  at proper time  $\tau_0 = 0.1$  fm/c with uniform pseudo-rapidity  $1/2 \log((t+z)/(t-z))$  distribution between  $|\eta| < 5$ . The transverse density distribution was assumed to be proportional to the binary collision distribution for two Woods-Saxon distributions. For collisions at impact parameter  $b$  the transverse binary collision profile is

$$\frac{dN(b)}{d^2x_T} = \frac{1}{2} \int_{-b}^b T_A(x_T) dx_T + \frac{b}{2} T_A(x_T) \frac{b}{2} \quad ; \quad (10)$$

where  $T_A(b) = \int_{-b}^b dz_A \rho_A(z^2 + b^2)$ , in terms of the diffuse nuclear density  $\rho_A(x)$ . The pQCD jet cross section normalization,  $\sigma_{jet}$ , and the temperature  $T_0$  were determined by fitting the gluon mini-jet transverse momentum spectrum predicted by HJING [21] for central Au+Au collisions at  $\sqrt{s} = 130$  A GeV (without shadowing and jet quenching). This gives  $dN(0)/d^2p_T = 210$  and  $T_0 = 700$  MeV.

Evolution from different initial densities (but the same density profile) can be obtained by varying the cross section only and using the scaling property explained in Section II C.

The evolution was performed numerically with 40 and 100 mb isotropic cross sections, and with 3, 40 and 100 mb gluonic cross sections with  $\beta = 1$ . We used particle subdivision  $\lambda = 100$  for impact parameters 0, 2, and 4 fm, while  $\lambda = 220, 450, 1100, \text{ and } 5000$ , for  $b = 6, 8, 10, \text{ and } 12$  fm.

As emphasized in the previous Section, we will label the results by the effective elastic transport opacity,  $\beta$ , from Eq. (7) and  $b$ . Table I shows  $\beta$  for each simulation, determined directly from the average number of cascade collisions per particle. In Table I we also introduced letter codes (A) through (F) as a quick reference to particular subsets of simulation parameters. We will include this letter code on most labels together with  $\beta$ , for convenience.

## A. Elliptic flow results

Figures 1 and 2 show the non-asymptotic gluon elliptic flow as a function of transverse momentum for different impact parameters. With increasing  $p_T$ , elliptic

flow increases until  $p_T \approx 1.5 - 2$  GeV, where it saturates, reproducing the pattern observed at RHIC. With increasing impact parameter, elliptic flow first monotonically increases, then monotonically decreases, showing a maximum at  $b \approx 8$  fm. These features were universal for all the cross sections we studied. Also, as expected, elliptic flow is a monotonically increasing function of the transport opacity, if the impact parameter is kept fixed.

Figure 3 shows the impact-parameter-averaged gluon elliptic flow as a function of transverse momentum for different transport opacities. The impact-parameter-averaged flow was computed via the formula

$$v_2(p_T) = \frac{2}{b_{max}^2} \int_0^{b_{max}} db b \frac{\int_{-b}^b d \cos(2\eta) \frac{dN}{d^2p_T}(b)}{\int_{-b}^b d \frac{dN}{d^2p_T}(b)} \quad ; \quad (11)$$

with  $b_{max} = 12$  fm. This, in fact, gives a somewhat smaller flow<sup>3</sup> than the minimum-bias elliptic flow defined by STAR as

$$v_2^{STAR}(p_T) = \frac{\int_0^{b_{max}} db b \int_{-b}^b d \cos(2\eta) \frac{dN}{d^2p_T}(b)}{\int_0^{b_{max}} db b \int_{-b}^b d \frac{dN}{d^2p_T}(b)} \quad ; \quad (12)$$

which weights flow in more central events preferentially.

Figure 4 shows that subdivision scaling (4), hence Lorentz covariance [17], is strongly violated for insufficient particle subdivision. For the initial conditions for Fig. 4 ( $b = 8$  fm,  $\beta = 487$ ), a particle subdivision  $\lambda = 200$  is needed to reduce numerical artifacts to a reasonable level. This also means that for  $b = 0, 2, \text{ and } 4$  fm,  $\lambda = 100$  is not sufficient if  $\beta > 4 - 5$ . Unfortunately, we could not afford a higher subdivision computationally.

Varying the magnitude of energy loss we searched for the drop in  $v_2(p_T)$  at high  $p_T$  predicted by calculations based on parton energy loss [12,13]. Although these studies consider radiative energy loss, one expects a similar behavior in case of purely elastic energy loss at the large opacities considered here.

Figure 5 shows the dependence of  $v_2(p_T)$  on the transport opacity for a fixed impact parameter. We varied the opacity by changing the screening mass  $\mu$ . As expected, elliptic flow decreases with decreasing  $\mu$ . However, there is no sign of a drop at high  $p_T$ : within statistical errors, the results are consistent with a constant flow from 2 to 6 GeV transverse momentum.

<sup>3</sup> This is opposite to the case of ideal hydrodynamics, where the STAR definition results in smaller flow. The main reason is the difference between the hydro and the cascade  $v_2(b)$  shape.

Figures 6 and 7 show the final gluon  $p_T$  spectra as a function of transport opacity and impact parameter. While Hijing densities with the pQCD elastic cross section are too dilute ( $\tau \approx 0.01 - 0.1$ ) to produce more than 10% quenching, as we increase the transport opacity, quenching "turns on" and by  $\tau \approx 7 - 8$  it is an order of magnitude at  $p_T > 6$  GeV.

Figure 10 shows that, unlike elliptic flow which is also driven by the spatial anisotropy, the relevant parameter that governs quenching is  $\tau$  alone. With 20% accuracy, simulations with very different impact parameters agree on the magnitude of quenching, provided  $\tau$  is the same.

While the quenching depends on  $\tau$  only, the absolute yield is proportional to the initial  $dN/d\eta$ . Hence from the absolutely normalized measured spectrum at a given centrality one could extract both  $\tau$  and  $dN(0)=d$ .

The  $p_T$  spectra are very sensitive to particle subdivision, as shown in Fig. 9. For insufficient subdivision, the high- $p_T$  spectrum is "reheated" during the expansion, which is clearly a numerical artifact. As the subdivision is increased, "reheating" disappears and, for the particular parameters ( $b = 8$  fm,  $\tau = 4.87$ ), the spectrum converges for  $N \approx 250$ .

### C. Transport opacity dependence

In this section we provide numerical evidence for the remarkable invariance of the results on the actual angular dependence of the differential cross section (2). Only the transport cross section moment, (3) seems to matter for the problem considered here as seen from Fig. 10.

The reason that this simplification occurs is that for the hadron and gluon energy range considered in these plots, the transport opacity is actually high enough, that little memory of the initial gluon momentum direction remains after multiple scattering. Thus isotropic scattering and  $\tau = T$  forward scattering both lead to essentially a random reorientation of all the gluons involved.

To see this in detail, we show in Fig. 12 that aside from a small 10% delta function component due to the gluons in the "corona" surface region that escape without rescattering, the bulk of the minijets undergo enough rescatterings that their final direction is randomized. In Fig. 11 we show that the rapidity shift of gluons in each transverse momentum interval considered has the form close to one expected if local thermal equilibrium occurred:

$$\begin{aligned} \frac{dP}{dy} &= \int dm_{\perp i}^2 dy_i dm_{\perp f}^2 \cos^2 \theta_i \cosh y_i m_{\perp f} \cosh(y_i + y) \\ &= \frac{1}{4T_i^3} \frac{1}{4T_f^3} e^{(m_{\perp i} \cosh y_i) = T_i} e^{(m_{\perp f} \cosh(y_i + y)) = T_f} \\ &= \frac{y \cosh y}{\sinh^3 y} : \end{aligned} \quad (13)$$

This final randomization of momentum is however not sufficient to ensure the validity of local equilibrium necessary for the applicability of non-dissipative Euler hydrodynamics. This can be seen from the dependence of the transverse momentum spectra and elliptic flow on the finite opacity parameter itself. In the hydrodynamic limit  $\tau = 1$  and as we showed in detail in a previous study [17], the solutions of the transport equations differ very much from ideal (Euler) hydrodynamics. While no covariant 3+1D Navier-Stokes solutions are yet known, our transport solutions demonstrate the effects of dissipation through their dependence on  $1/\tau$ , which is effectively a measure of the importance of viscosity.

The invariance of the transport solutions to the angular distributions for a fixed  $\tau$  indicate however that we are not extremely far from the local thermal although dissipative limit. In particular these solutions are far from the Eikonal (Kudsen) type dynamics as considered for example in [13].

A criterion for the validity of the Eikonal approximation is that the angle between the initial and final parton momenta satisfies  $\theta < 1$ , say  $\theta < 0.1$ . For an energetic parton that undergoes  $N$  elastic collisions, this angle can be approximated in an analogous way to random walk as

$$\theta_i \approx \frac{q}{N \hbar \sin^2 \theta_{cm i}} = P^{-1}; \quad (14)$$

where we used Eqs. (3) and (7) in the last step. Hence, for elastic collisions, Eikonal approximation is valid only for very small  $\theta < 0.01$  transport opacities. Even in the most optimistic  $N = 1$  case, this condition is satisfied only for  $z^2 = s < 4 \cdot 10^4$ . For collisions with typical thermal partons ( $s \approx 6ET$ ,  $\theta = T$ ), this requires parton energies  $E > 500T$ , i.e., several hundred GeV in our case.

Similar considerations hold for  $N > 1$  as well because the total cross section does not depend on the parton energy and therefore the number of collisions is approximately independent of energy. In Fig. 12 we demonstrate that the Eikonal limit becomes more applicable as the parton energy increases. The higher the initial  $p_T$ , the less change occurs in the parton direction during the whole evolution. Of course, the trend is weak because the transverse momentum we could consider were orders of magnitude below the 100 - 1000 GeV regime.

What we see with these results is that the pattern of "jet quenching", as observed at RHIC via the suppression of moderate transverse momentum particles and the saturation of elliptic flow above some critical  $p_T$ , can be reproduced if sufficiently high transport opacities are postulated.

## IV. RESULTS FOR HADRONS

The results in the previous Section pertain to the partonic world. To compare with experimental results, we

have to model hadronization. Here we compute the hadronic observables from two different hadronization schemes.

#### A. Hadronization via local parton-hadron duality

A simple hadronization model can be constructed based on local parton-hadron duality. Following Ref. [22], we simply assume that each gluon gets converted to a pion with equal probability for the three isospin states. Since most hadrons are pions, we approximate the transverse momentum distribution of negative charged hadrons with that of the negative pions as

$$f_h(p_T) = f_\pi(p_T) = \frac{1}{3}f_g(p_T): \quad (15)$$

With the above prescription, elliptic flow does not change during hadronization, i.e., Figs. 1{5 show the negative hadron flow as well. Furthermore, the negative hadron  $p_T$  spectra can be obtained from Figs. 6{9 via simply dividing by 3. Consequently, the scaling (9) holds for the negative hadron flow and spectra as well.

In Fig. 3, the elliptic flow data by STAR are reproduced with a transport opacity  $\tau_{b=0} = 23.9$ . For an initial gluon density  $dN_g(0) = d = 1000$ , this corresponds to  $\tau = 14$  mb, i.e., to a total cross section of  $\sigma_0 = 45$  mb with  $\tau = T_0$ . If we took the pQCD  $gg$  cross section of 3 mb with  $\tau = T_0$ , this opacity would correspond to an initial gluon density of  $dN_g(0) = d = 15000$  that is contradicted by the much smaller observed  $dN_{ch} = d = 600$ .

The  $p_T$  spectra provide a much stronger constraint on the initial gluon density as their absolute magnitude is proportional to it. At high opacities ( $\tau > 5$ ), the need for high particle subdivisions poses a severe computational problem, therefore we can reliably compute particle spectra for semi-central collisions only. Nevertheless, the data measured by STAR in central collisions, where quenching due to parton energy loss is expected to be maximal, provides an important lower bound on the particle yields. Figure 6 shows that the elastic transport opacities  $\tau < 10$  considered here are compatible with this lower bound.

On the other hand, the cascade semi-central results seem to be too far above the central measurements. It is unlikely that going from semi-central to central collisions would give us an order of magnitude or more increase in quenching needed to reach the central STAR data. Either much higher opacities  $\tau > 10$  than those considered in this study would be needed to reach the central data, or it may even be that with this hadronization scheme it is not possible to reproduce the data even in the  $\sqrt{s} = 1$  hydrodynamic limit.

#### B. Hadronization via independent fragmentation

Another possible hadronization scheme is to fragment the gluons as independent jets. Since the majority of the hadrons are pions, we consider only the  $g \rightarrow \pi$  channel with the next-to-leading-order fragmentation function computed in Ref. [29]. We take the scale factor  $s = \log(Q^2) = \log(Q_0^2)$  to be zero because the initial HJING gluon distribution is already quenched due to initial and final state radiation. Also, since we do not consider soft physics, we limit our study to hadrons with  $p_T > 2$  GeV and hence fragment gluons with  $p_T > 2$  GeV only.

Figure 13 shows the central in-pair-parameter-averaged negative hadron flow as a function of the transport opacity. The flow pattern and the magnitude of the flow are much the same as for partons in Fig. 3. Hence, we get the same constraint on the initial parameters as for hadronization via local parton-hadron duality. In the  $p_T < 2$  GeV region this simple calculation does not reproduce the data because it does not include contributions coming from soft physics.

The  $p_T$  spectra of charged hadrons are shown as a function of the elastic  $gg$  cross section and in-pair parameter in Figs. 14 and 15. In addition to quenching because of energy loss, the central pion spectra are further quenched due to independent fragmentation. With this additional quenching, the parton cascade results approach the STAR data, as indicated in Fig. 16 for rather extreme  $\sigma_0(\tau = T) = 100$  mb if HJING  $dN_g = dy = 210$  is assumed or if  $\sigma_0 = 25$  mb for EKRT  $dN_g = dy = 1000$  is assumed. These elastic cross sections exceed the conventional few mb pQCD cross sections at this scale by at least an order of magnitude.

## V. CONCLUSIONS

We applied the MPC parton cascade algorithm to solve covariant Boltzmann transport and compute specific new observables at RHIC. Our focus was on the recently measured differential elliptic flow and charged hadron  $p_T$  spectra. We also explored the difference between hadronization schemes based on independent fragmentation and local parton-hadron duality.

Our main result is that extremely large densities and/or elastic parton cross sections,  $\tau_{tot} dN = d = 80$  times the HJING estimate, are needed to reproduce the elliptic flow data [16]. Hadronization via local parton-hadron duality does not reproduce the rapid fall seen in the spectra at high  $p_T$ . However, the charged hadron  $p_T$  spectra obtained after hadronization via independent fragmentation compare well to the measured spectra as long as such extreme elastic transport opacities are postulated.

The results also demonstrate clearly how finite relation rates in A + A manifest in major deviations from hydro-

dynamic transverse flow effects at transverse momentum  $p_T > 2$  GeV. The pattern of quenching found with MPC is surprisingly similar to that obtained in the two component model of GVW [13]. The main difference between the MPC results presented here and those of GVW is that the latter include an estimate for radiative energy loss in an Eikonal formalism and a phenomenological "hydrodynamic" component. It is known that radiative energy loss of ultra-relativistic partons is much larger than elastic energy loss in a medium with a fixed density. In GVW the same quenching pattern was obtained with more modest initial densities  $dN_g/dy \approx 500$  using small pQCD elastic rates because the induced gluon radiation associated with multiple elastic collisions is large enough to compensate for the relatively small elastic transport opacity. In MPC the same level of quenching can only be achieved by increasing the elastic opacity artificially by an order of magnitude. Therefore the present study confirms the expectation that elastic scattering alone is not enough to generate the degree of collectivity observed now at RHIC.

## V I. O U T L O O K

The results presented here underscore the urgent need to develop practical convergent algorithms to incorporate inelastic  $2 \leftrightarrow 3$  processes. Preliminary work in Ref. [19] indicated a rather slow convergence towards Lorentz covariance using the particle subdivision technique. Unlike the  $\lambda^{-1=2}$  convergence in  $2 \leftrightarrow 2$ , a much slower  $\lambda^{-1=5}$  convergence is expected in  $2 \leftrightarrow 3$  processes even when nonlocal formation physics ( $t > h = E$ ) is neglected.

In addition, a covariant approximation to Boltzmann transport theory is needed to overcome the overwhelming computational difficulty in the high opacity regime even for elastic scattering where particle subdivisions of several hundred to thousand are required.

Finally, we note that all results in this paper pertain to homogeneous initial conditions. In Ref. [30], it was shown that jets induce large nonstatistical local fluctuations that may evolve in a turbulent manner. A transport study of the evolution from such inhomogeneous initial conditions would be interesting to compare to the known hydrodynamic solutions.

## V I I. A C K N O W L E D G M E N T S

We acknowledge the Parallel Distributed Systems Facility at the National Energy Research Scientific Computing Center for providing computing resources. We thank RMKIKFKI for hospitality during the completion of this work.

This work was supported by the Director, Office of Energy Research, Division of Nuclear Physics of the Office of High Energy and Nuclear Physics of the U.S. Department of Energy under contract No. DE-FG-02-93ER-40764.

M.G. also was partially supported by the Collegium Budapest.

- 
- [1] H. Stoecker and W. Greiner, Phys. Rept. 137, 277 (1986)
  - [2] J. Ollitrault, Phys. Rev. D 46, 229 (1992).
  - [3] H. Sorge, Phys. Rev. Lett. 78, 2309 (1997) [nucl-th/9610026];
  - [4] H. Sorge, Nucl. Phys. A 661, 577 (1999) [nucl-th/9906051].
  - [5] S. Voloshin and Y. Zhang, Z. Phys. C 70, 665 (1996) [hep-ph/9407282]; A.M. Poskanzer and S.A. Voloshin, Phys. Rev. C 58, 1671 (1998) [nucl-ex/9805001]; S.A. Voloshin and A.M. Poskanzer, Phys. Lett. B 474, 27 (2000) [nucl-th/9906075].
  - [6] P. F. Kolb, U. Heinz, P. Huovinen, K. J. Eskola and K. Tuominen, hep-ph/0103234; P. Huovinen, P. F. Kolb, U. Heinz, P. V. Ruuskanen and S. A. Voloshin, Phys. Lett. B 503, 58 (2001) [hep-ph/0101136]; P. F. Kolb, P. Huovinen, U. Heinz and H. Heiselberg, Phys. Lett. B 500, 232 (2001) [hep-ph/0012137]; P. F. Kolb, J. Sollfrank and U. Heinz, Phys. Lett. B 459, 667 (1999) [nucl-th/9906003].
  - [7] L. P. Csernai and D. Rohrlich, Phys. Lett. B 458, 454 (1999) [nucl-th/9908034].
  - [8] D. Teaney, J. Lauret and E. V. Shuryak, nucl-th/0011058.
  - [9] B. Zhang, M. Gyulassy and C.M. Ko, Phys. Lett. B 455, 45 (1999) [nucl-th/9902016].
  - [10] E. E. Zabrodin, C. Fuchs, L. V. Bravina and A. Faessler, nucl-th/0006056.
  - [11] M. Bleicher and H. Stoecker, hep-ph/0006147.
  - [12] X. Wang, nucl-th/0009019.
  - [13] M. Gyulassy, I. Vitev and X. N. Wang, Phys. Rev. Lett. 86, 2537 (2001), [nucl-th/0012092].
  - [14] K. H. Ackermann et al. [STAR Collaboration], Phys. Rev. Lett. 86, 402 (2001) [nucl-ex/0009011].
  - [15] H. Appelshauser et al. [NA 49 Collaboration], Phys. Rev. Lett. 80, 4136 (1998) [nucl-ex/9711001].
  - [16] R. J. Snellings [STAR Collaboration], nucl-ex/0104006.
  - [17] D. Molnar and M. Gyulassy, Phys. Rev. C 62, 054907 (2000) [nucl-th/0005051].
  - [18] B. Zhang, M. Gyulassy and C.M. Ko, Phys. Lett. B 455, 45 (1999) [nucl-th/9902016].
  - [19] D. Molnar, in Proceedings of Quark Matter '99 Int. Conference on Ultra-relativistic Nucleus-Nucleus Collisions, Torino, Italy, May 10-15, 1999, eds. L. Roccoati, M. M. Asara, E. Vercellin, p. 236c.
  - [20] D. Molnar and M. Gyulassy, nucl-th/0102031.
  - [21] M. Gyulassy and X. Wang, Comput. Phys. Commun. 83, (1994) 307 [nucl-th/9502021].
  - [22] K. J. Eskola, K. Kajantie, P. V. Ruuskanen, and K. Tuominen, Nucl. Phys. B 570, 379 (2000) [hep-ph/9909456].
  - [23] D. Molnar, MPC 1.0.6. This parton cascade code used in the present study can be downloaded from WWW at

<http://nt3.phys.columbia.edu/people/mohard>.

- [24] B. Zhang, *Comput. Phys. Commun.* 109, 193 (1998) [nucl-th/9709009].
- [25] M. Gyulassy, Y. Pang, and B. Zhang, *Nucl. Phys. A* 626, (1997) 999.
- [26] B. Zhang, M. Gyulassy, and Y. Pang, *Phys. Rev. C* 58, (1998) 1175 [nucl-th/9801037].
- [27] Y. Pang, RHIC 96 Summer Study, CU-TP-815 preprint (unpublished); Generic Cascade Program (GCP) documentation available at WWW site <http://rhic.phys.columbia.edu/rhic/gcp>.
- [28] Proceedings of Open Standards for Cascade Models for RHIC (OSCAR), BNL-64912, June 23-27, 1997, eds. Miklos Gyulassy and Y. Pang; Source codes and documentation for transport models under the OSCAR standard can be downloaded from the OSCAR WWW site <http://rhic.phys.columbia.edu/rhic/>.
- [29] J. Binnewies, B. A. Kniehl and G. Kramer, *Z. Phys. C* 65, 471 (1995) [hep-ph/9407347].
- [30] M. Gyulassy, D. Rischke, and B. Zhang, *Nucl. Phys. A* 613 (1997) 397.

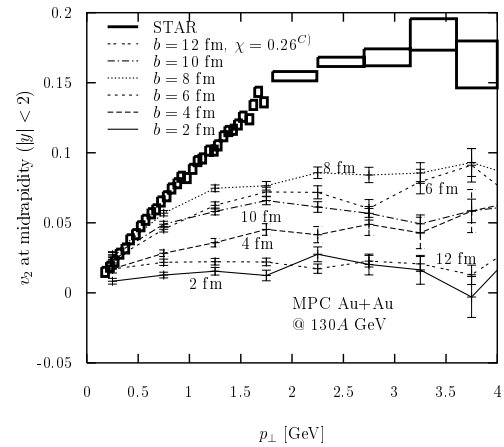


FIG. 1. Gluon elliptic flow as a function of  $p_T$  for Au+Au at  $\sqrt{s} = 130A$  GeV with impact parameters  $b = 2, 4, 6, 8, 10,$  and  $12$  fm (transport opacities = 3.95, 3.49, 2.84, 1.95, 0.99, and 0.26).

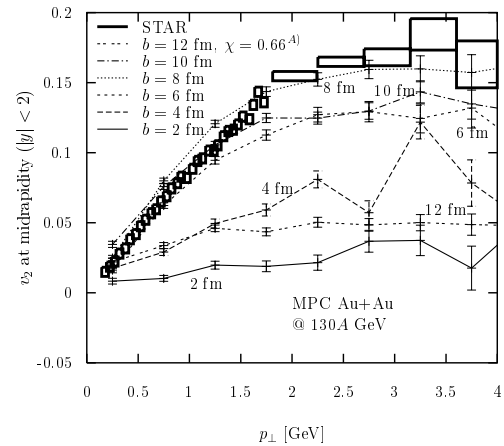


FIG. 2. Gluon elliptic flow as a function of  $p_T$  for Au+Au at  $\sqrt{s} = 130A$  GeV with impact parameters  $b = 2, 4, 6, 8, 10,$  and  $12$  fm (transport opacities = 9.72, 8.61, 7.05, 4.87, 2.50, and 0.66).

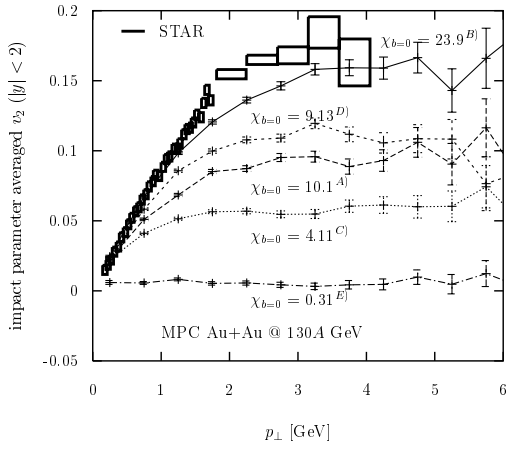


FIG. 3. Impact parameter averaged gluon elliptic flow as a function of  $p_{\perp}$  for Au+Au at  $\sqrt{s} = 130A$  GeV with transport opacities  $\chi_{b=0} = 0.31, 4.11, 9.13, 10.1$  and  $23.9$  for  $b=0$ . Identical to the charged hadron elliptic flow if the gluons are hadronized via local parton-hadron duality.

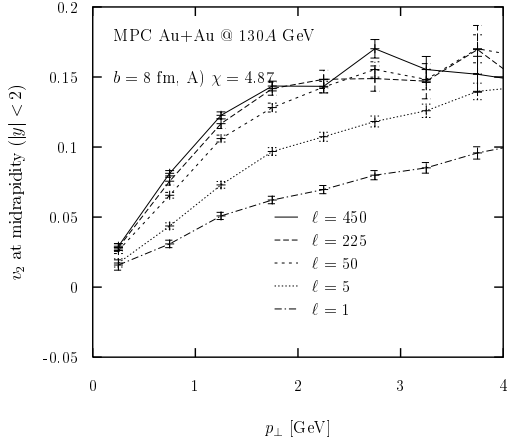


FIG. 4. Gluon elliptic flow as a function of  $p_{\perp}$  for Au+Au at  $\sqrt{s} = 130A$  GeV with  $b=8$  fm,  $\chi = 4.87$ , and particle subdivisions  $\ell = 1, 5, 50, 225$ , and  $450$ .

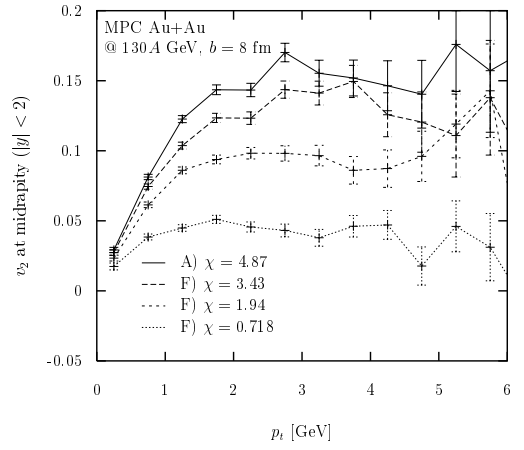


FIG. 5. Gluon elliptic flow as a function of  $p_{\perp}$  for Au+Au at  $\sqrt{s} = 130A$  GeV with  $b=8$  fm and  $\tau_0 = 0.226, 0.45, 0.71$ , and  $1$  ( $\chi = 0.718, 1.94, 3.43$ , and  $4.87$ ).

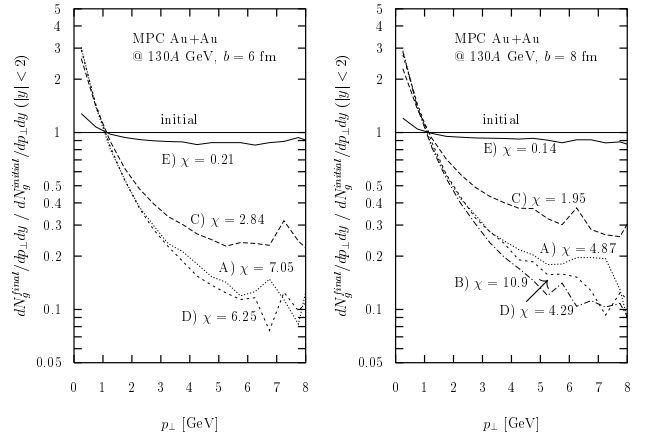


FIG. 6. Final gluon  $p_{\perp}$  spectra relative to the thermal initial spectrum as a function of transport opacity for Au+Au at  $\sqrt{s} = 130A$  GeV with  $b=6$  fm (left) and  $b=8$  fm (right).

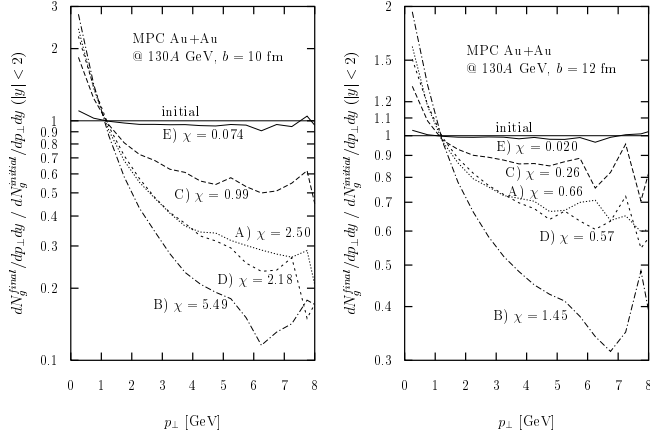


FIG . 7. Same as Fig. 6, except with  $b = 10$  fm (left) and  $b = 12$  fm (right).

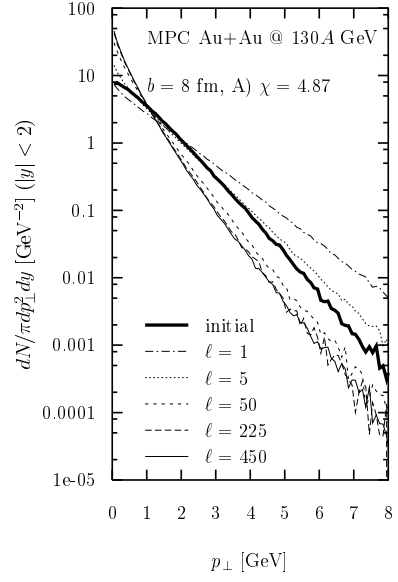


FIG . 9. Final gluon  $p_{\perp}$  spectra for Au+Au at  $\sqrt{s} = 130.4$  GeV with  $b = 8$  fm,  $\chi = 4.87$ , and particle subdivisions  $\ell = 1, 5, 50, 225,$  and  $450$ . The spectra are plotted for  $dN(0) = d = 210$ .

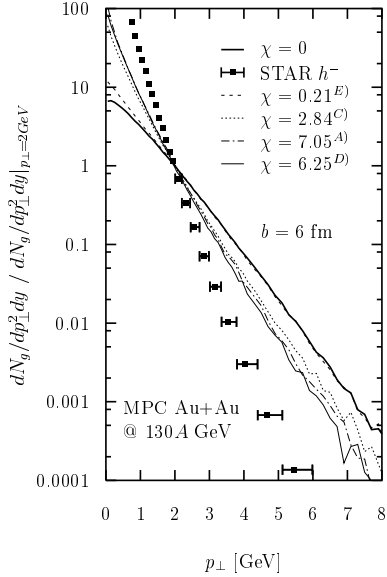


FIG . 8. Same as the curves for  $b = 6$  fm in Fig. 6 but with all curves normalized to 1 at  $p_{\perp} = 2$  GeV. This shows the quenching at high  $p_{\perp}$  relative to  $p_{\perp} = 2$  GeV.

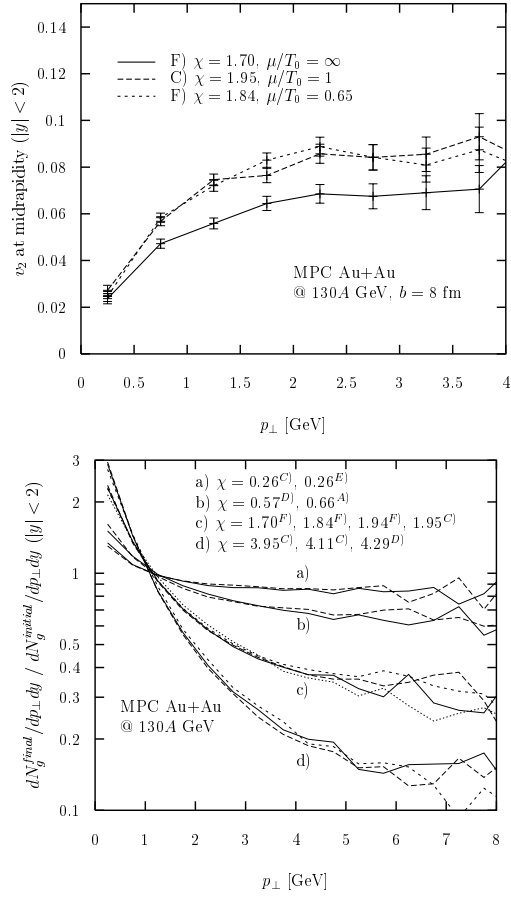


FIG .10. Transport opacity dependence of elliptic flow and the  $p_T$  spectra.

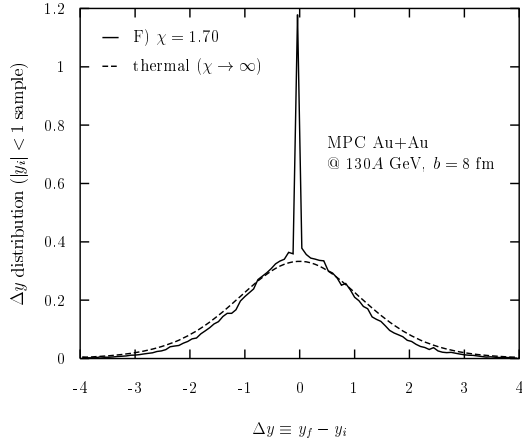


FIG .11. Correlation between initial and final rapidity.

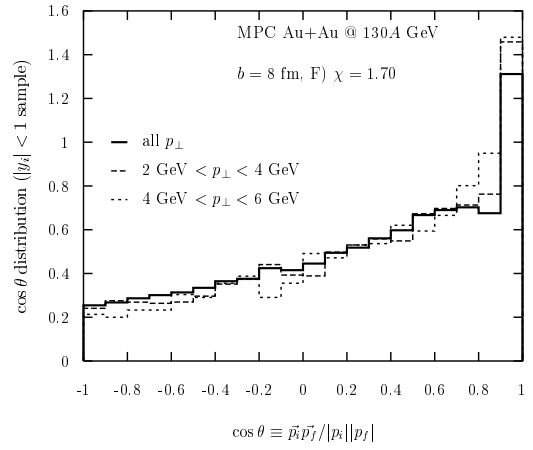


FIG .12. Correlation between initial and final momentum direction.

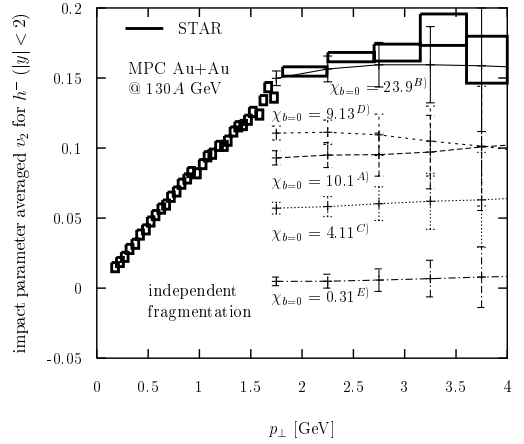


FIG .13. Impact parameter averaged negative hadron elliptic flow as a function of  $p_T$  for Au+Au at  $\sqrt{s} = 130$  A GeV with transport opacities  $\chi_{b=0} = 0.31, 4.11, 9.13, 10.1$  and  $23.9$  at  $b = 0$  and hadronization via independent fragmentation. The  $p_T < 2$  GeV region is not plotted because it is dominated by soft contributions not addressable via pQCD jet fragmentation physics.

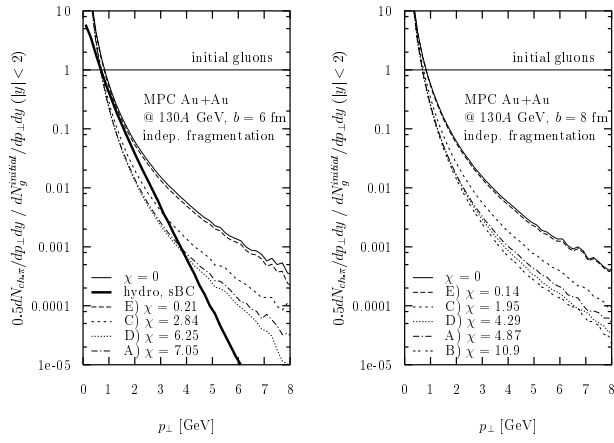


FIG. 14. Final negative hadron  $p_T$  spectra via independent fragmentation relative to the thermal initial gluon spectrum for Au+Au at  $\sqrt{s} = 130A$  GeV with  $b = 6$  fm (left) and  $b = 8$  fm (right). The ideal hydrodynamics result in the left figure is taken from [6] with the so called sBC initial conditions. It was extrapolated beyond  $p_T = 3$  GeV using an exponential  $t$  to the  $dN/dp_T dp_T$  distribution between 2 and 3 GeV.

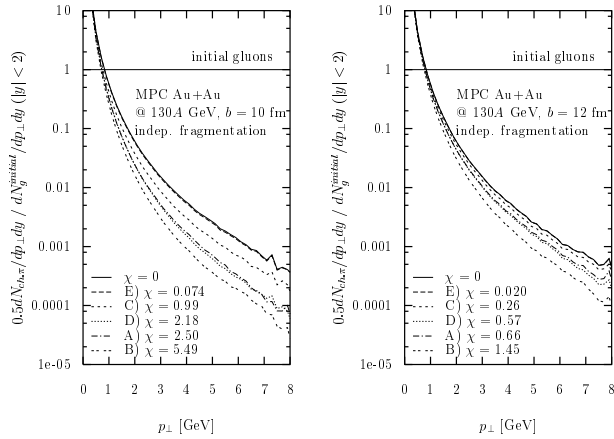


FIG. 15. Same as Fig. 14, except with  $b = 10$  fm (left) and  $b = 12$  fm (right).

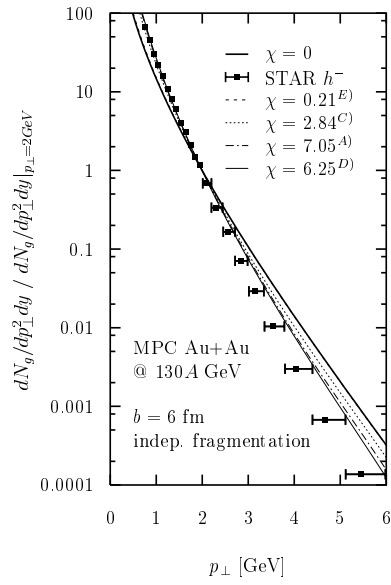


FIG. 16. Same as the curves for  $b = 6$  fm in Fig. 14 but with all curves normalized to 1 at  $p_T = 2$  GeV. This shows the quenching at high  $p_T$  relative to  $p_T = 2$  GeV.

A) $\tau_0 = 100$ mb, $T_0 = 1$			B) $\tau_0 = 100$ mb, $T_0 = 0$		
b [fm]	h <i>i</i>		b [fm]	h <i>i</i>	
0	33.0	10.1	0	35.8	23.9
2	31.7	9.72	2	34.3	22.9
4	28.1	8.61	4	30.2	20.1
6	23.0	7.05	6	24.0	16.0
8	15.9	4.87	8	16.3	10.9
10	8.16	2.50	10	8.23	5.49
12	2.15	0.66	12	2.18	1.45
C) $\tau_0 = 40$ mb, $T_0 = 1$			D) $\tau_0 = 40$ mb, $T_0 = 0$		
b [fm]	h <i>i</i>		b [fm]	h <i>i</i>	
0	13.4	4.11	0	13.7	9.13
2	12.9	3.95	2	13.2	8.80
4	11.4	3.49	4	11.6	7.73
6	9.26	2.84	6	9.38	6.25
8	6.37	1.95	8	6.44	4.29
10	3.23	0.99	10	3.27	2.18
12	0.86	0.26	12	0.86	0.57
E) $\tau_0 = 3$ mb, $T_0 = 1$			F) various, $b = 8$ fm		
b [fm]	h <i>i</i>		$\tau_0$ [fm]	$T_0 =$	h <i>i</i>
0	1.00	0.31	60	1.54	9.51 1.84
2	0.96	0.29	16	0	2.55 1.70
4	0.85	0.26	100	1.40	15.9 3.43
6	0.69	0.21	100	2.21	15.7 1.94
8	0.47	0.14	100	4.43	15.5 0.718
10	0.24	0.074			
12	0.064	0.020			

TABLE I. Parameters and transport opacity for each transport solution computed via MPC for the present study.